Drift-Diffusion Modeling of the Effects of Structural Disorder and Carrier Mobility on the Performance of Organic Photovoltaic Devices

Benjamin Y. Finck* and Benjamin J. Schwartz†

Department of Chemistry and Biochemistry, UCLA, Los Angeles, California 90095-1569, USA

(Received 22 April 2015; revised manuscript received 27 July 2015; published 21 September 2015)

We probe the effects of structural disorder on the performance of organic photovoltaic (OPV) devices via drift-diffusion modeling. We utilize ensembles of spatially disordered one-dimensional mobility profiles to approximate the three-dimensional structural disorder present in actual devices. Each replica in our ensemble approximates one high-conductivity pathway through the three-dimensional network(s) present in a polymer-based bulk heterojunction solar cell, so that the ensemble-averaged behavior provides a good approximation to a full three-dimensional structurally disordered device. Our calculations show that the short-circuit current, fill factor, and power conversion efficiency of simulated devices are all negatively impacted by the inclusion of structural disorder, but that the open-circuit voltage is nearly impervious to structural defects. This is in contrast to energetic disorder, where previous studies found that spatial variation in the energy in OPV active layers causes a decrease in the open-circuit voltage. We also show that structural disorder causes the greatest detriment to device performance for feature sizes between 2 and 10 nm. Since this is on the same length scale as the fullerene crystallites in experimental devices, it suggests both that controlling structural disorder is critical to the performance of OPV devices and that the effects of structural disorder should be included in future drift-diffusion modeling studies of organic solar cells.

DOI: 10.1103/PhysRevApplied.4.034006

I. INTRODUCTION

Organic photovoltaic (OPV) technology has seen marked improvement in recent years, with device power conversion efficiencies (PCEs) surpassing 11% [1]. The most efficient devices are constructed from blends of a semiconducting polymer, which acts as the light absorber and hole transporter, and a fullerene derivative, which serves to separate the excitons created on the polymer and to transport the electrons. Such polymer:fullerene mixtures, known as bulk heterojunctions (BHJs), must be both intimately blended to assure good charge separation, yet phase separated enough to ensure that there are physically continuous conducting pathways for both the electrons and holes to reach their respective electrodes [2]. The BHJ morphology, however, is difficult to control, and as a result, the relationship between the morphology of the disordered donor-acceptor blends in OPVs and the underlying mechanisms of charge generation, recombination, and transport in such disordered systems is not well understood [3].

In addition to all of the experiments that have been performed to elucidate structure-property relationships in OPVs, there also has been a significant amount of theoretical work, particularly in the field of device modeling [4–6]. The most commonly employed approach is the drift-diffusion (DD) model, which has been utilized to simulate a wide variety of OPV-device physics experiments, such as current-density–voltage (J-V) characteristics, photogenerated charge extraction by linearly increasing voltage (photo-CELIV), transient photocurrent measurements, etc. [7–9]. One feature that is often neglected in DD simulations, but is of particular importance for OPV devices, is the role of disorder of the organic active layer. Most DD simulations treat the BHJ blend as a uniform, continuous medium that is characterized by a single mobility for each carrier [4,5,10–13]. Disorder has been accounted for primarily from the perspective of energetic disorder in BHJ blends, which arises from the fact that the polymers in OPV active layers twist and bend along their conjugated backbone and the fact that both the polymer and fullerenes in BHJ blends reside in distinct chemical environments [14,15]. Several groups have modeled this energetic disorder by including a Gaussian-shaped density of energy states in their DD simulations, which affects both carrier mobility and recombination [14,15]. In addition to a Gaussian distribution, groups also have considered an exponential distribution of trap states [16–18]. These groups find that the simulated performance of devices with energetic disorder is reduced as a result of diminished short-circuit current, fill factor, and open-circuit voltage.

Despite the progress made towards understanding the role of energetic disorder in BHJ devices, few drift-diffusion simulations have addressed the structural disorder that is also present in BHJ devices or how this disorder impacts carrier transport. By structural disorder, we mean the random spatial distribution of polymers and fullerenes

*bfinck@chem.ucla.edu
†schwartz@chem.ucla.edu

that is found in a BHJ, resulting in tortuous pathways for carrier transport. The existence of structural disorder clearly affects the net carrier mobility. For example, many experiments, including photo-CELIV, transient photocurrent, and space charge limited-current measurements, have shown that on device length scales, the carriers in polymer:fullerene OPVs have relatively low mobilities, on the order of 10^{-4} $cm^2\,V^{-1}\,s^{-1}$ [19–21]. In contrast, time-resolved microwave conductivity (TRMC) measurements indicate that over short length scales, the photogenerated charge carriers in these systems have relatively high mobilities ($\sim 10^{-2}$ $cm^2\,V^{-1}\,s^{-1}$), comparable to what is seen in FET-based mobility measurements [22–24]. Clearly, when carriers move on length scales that sample the spatial disorder inherent in BHJ OPV devices, the result is a lowering of the effective carrier mobility by roughly 2 orders of magnitude. These differences in mobility at varying length scales can be understood from the fact that intrachain transport is characterized by significantly higher mobility than interchain hopping, yet interchain hopping is the dominant transport mechanism for disordered semiconducting polymers [25,26]. All of this suggests that due to structural disorder, the conducting pathways in a BHJ have a distribution of regions with high and low carrier mobility, as opposed to a single continuous mobility.

Structural measurements based on X-ray diffraction and various microscopies have indicated that both the polymers and fullerenes in a BHJ phase segregate into crystallites with sizes on the order of several nanometers, with amorphous and potentially intermixed regions surrounding the crystallites [27–31]. This means that structural disorder is inherent to polymer:fullerene OPVs. The goal of this work is to use DD modeling specifically to understand the effects of this structural disorder on the performance of BHJ photovoltaic devices. We note that previous studies that have included a functional dependence of mobility on factors such as the electric field, carrier density, or the energetic density of states, have still been limited to smooth, non–spatially-varying mobility profiles and thus have not accounted for the spatial distribution of conductivities present in a BHJ architecture [14,32,33]. This means that previous studies have not considered how the grain boundaries between conducting materials or between crystalline and amorphous regions affect mobility and obstruct charge transport. It is clear that to accurately model a BHJ device, one should consider structural disorder in addition to energetic disorder.

In this work, we present an approach to account for structural disorder in 1D drift-diffusion modeling of OPV devices. Our work at this stage intentionally neglects the effects of energetic disorder, which would be expected to accompany structurally disordered morphologies, in order to isolate the effects of structural disorder alone on OPV-device physics. We present two methods for generating spatially disordered mobility profiles: one method where each profile is generated by random sampling from a probability distribution of possible carrier mobilities, and a second method where profiles are generated from the disordered morphologies generated by Cahn-Hilliard (CH) modeling [34,35]. Both sampling methods result in mobility profiles that contain regions of exceptionally high and/or low mobilities for the carriers. A high-mobility region represents transport along a single chain or through a region of the material with high crystallinity and thus high carrier conductivity. Conversely, a low-mobility region represents transport of a carrier through the "wrong" conducting material or through a grain boundary or defect, or represents the occurrence of dead ends and other features of the meandering conduction pathways present in BHJ architectures [36]. Our method then treats devices as ensembles of these 1D disordered-carrier pathways.

We demonstrate that as the parameters for both methods (the characteristics of the mobility distribution and the parameters used to transform the 1D CH morphologies into structurally disordered mobility profiles) are varied, there are profound effects on the resulting performance of the ensemble-averaged modeled disordered devices. We also show that no matter how the disordered mobility profiles are generated, the resultant effects on device performance are similar, indicating that our findings are robust to the details of how structural disorder is included in drift-diffusion simulations. Our simulations show that, similar to studies of energetic disorder, structural disorder leads to an overall degradation of device performance, particularly in regards to the short-circuit current (J_{SC}) and fill factor (FF). However, unlike studies on energetic disorder, we do not find a significant degradation of the open-circuit voltage (V_{OC}), and we discuss in detail the reasons why structural disorder has these particular effects on device performance. We also see that the length scale of disorder is important, with the most severe effects on device performance accompanying disorder on length scales of $\sim$10 nm, exactly the size expected in real BHJ OPV devices.

II. COMPUTATIONAL METHODS

A. Drift diffusion model

For this work, we perform all of our device simulations using the DD model, in which the electron and hole current densities are treated as

$$J_n = -qn\mu_n\nabla V + kT\mu_n\nabla n, \tag{1}$$

$$J_p = -qp\mu_p\nabla V - kT\mu_p\nabla p, \tag{2}$$

where q is the fundamental charge, V is the electrostatic potential, n and p refer to the electron and hole densities, and μ_n and μ_p refer to the mobility of electrons and holes, respectively [32]. In order to simulate a device, one needs to solve the continuity equations for both carriers:

$$\frac{\partial n}{\partial t} = \frac{1}{q}\nabla J_n - R + G, \tag{3}$$

$$\frac{\partial p}{\partial t} = -\frac{1}{q}\nabla J_p - R + G, \tag{4}$$

where R is the net recombination rate of electrons and holes, which we treat with Langevin recombination of the form $R(x) = (q/\epsilon_r\epsilon_0)(\mu_n + \mu_p)np$, where ϵ_r is the dielectric constant of the medium and ϵ_0 is the vacuum permittivity. The G term in Eq. (3) is the generation profile within the active layer of the device. Since free carriers are assumed to be generated primarily as a result of photon absorption, we calculate this generation profile via a transfer-matrix formalism to account for thin-film interference and the absorption or refraction of light by the various layers of an OPV device [37]. To solve the above carrier-continuity equations, they need to be coupled through the Poisson equation

$$\nabla^2 V = \frac{q}{\epsilon_r\epsilon_0}(n - p). \tag{5}$$

The set of Eqs. (1)–(5) forms the basis of the drift-diffusion model.

We used the Gummel method to decouple the above set of partial-differential equations and solve the DD model in an iterative matter [38–41]. Our simulations provide a 1D model for a typical OPV architecture, where the organic active layer is sandwiched between two metal contacts. The drift-diffusion model equations are solved numerically for this active layer by discretizing the equations on a finite difference mesh. Because our structural-disorder model examined the effects of feature sizes of only a few nanometers, we tested grid spacings as low as 0.1 nm, but found that as long as the mesh size is less than $1/4$ of the disorder length scale, the results are numerically robust. Thus, in most of what is shown below, a 1-nm mesh spacing is used. As boundary conditions for the carrier-density equations, we assume thermionic injection at the metal-organic semiconductor interfaces [42]. As boundary conditions for the Poisson equation, we assume that the voltage drop across the device is equal the built-in voltage. We chose the other device parameters to be comparable to those previously used in the literature, and all the parameters we used in our calculations are collected in Table I. Additional computational details regarding our DD simulations are given in the Supplemental Material [43].

We note that similar approaches for OPV-device modeling based on the DD model have been previously implemented by many groups with great success [4,5,14,32]. The primary difference between the previous studies and ours is the explicit inclusion of spatially dependent carrier mobilities (μ_n and μ_p). The vast majority of previous 1D drift-diffusion studies have simply assumed a constant mobility value for electrons and holes, without taking into account the meandering conduction pathways (i.e., structural disorder) that carriers are known to traverse in a BHJ architecture. Spatial disorder of the mobility profiles has its greatest effect through the current gradient terms of Eqs. (3) and (4), as both the drift and diffusion current contributions are proportional to the carrier mobilities. The recombination rate also will be affected due to its functional dependence on the structurally disordered mobility profiles. The generation of free carriers also should be dependent on morphology, since carriers should be predominantly generated near the interface of the donor and acceptor materials. However, we have chosen to neglect the spatial dependence of free-carrier generation on the mobility profile for these simulations and instead assume an effective medium approach via the transfer-matrix formalism. We believe this is a reasonable approximation since the diffusion length of excitons in OPV materials (~10 nm) [44] is generally larger than the feature sizes considered in our disordered mobility profiles.

TABLE I. The boundary conditions and parameters used for the DD simulations presented in the figures, except where otherwise noted.

Parameter	Symbol	Value
Active layer thickness	d	100 nm
Relative permittivity	ϵ_r	3.5
Schottky injection barriers	ϕ_n, ϕ_p	0.3 eV
Langevin reduction factor	γ	0.1
Built-in voltage	V_{BI}	0.6 V
Effective density of states	N_C, N_V	1×10^{20} cm^{-3}
Temperature	T	298 K
Band gap	E_g	1.2 eV

B. Disordered mobility profiles and ensembles

1. Random sampling from a mobility distribution

As one way to approximate structural disorder in one dimension, we utilize an ensemble of spatially variable mobility profiles. To create such an ensemble, we first generate mobility profiles by randomly sampling mobility values from a distribution of possible mobilities. We will discuss the details of this distribution shortly. Starting from one end of the device and progressing to the opposite end, we assign a randomly sampled mobility value every δ nm to each of our carrier mobility (μ_n and μ_p) profiles. Our motivation for choosing spatially dependent mobility profiles in this way is based on the fact that a charge carrier moving through a disordered BHJ architecture can be expected to encounter many potential obstacles, such as grain boundaries, different conducting components, amorphous regions, and structural dead ends where the charge carrier is no longer capable of conducting through a continuous pathway towards its extraction contact without reversing direction. Experimental measurements have

shown that carrier conduction through the "wrong" conducting material (i.e., holes through the fullerene or electrons through the polymer) has an effective mobility that is several orders of magnitude lower than carrier mobility through the "correct" conducting material [45,46]. Thus, while traversing even the most conductive possible pathway(s) through an OPV device, a carrier may experience a range of mobilities that varies by several orders of magnitude.

It is worth noting that simple distributions, such as a Gaussian distribution, cannot generate mobilities that sample such a large range. Instead, we chose the exponent of the mobility distribution to be Gaussian to provide a way to generate random mobility profiles that span several orders of magnitude. In this way, we create mobility profiles such that

$$\mu_{n,p}(x) = 10^{[\mu_0 + \sigma Y(x)]} \tag{6}$$

where $Y(x)$ is a normally distributed random variable that determines the mobility at spatial position x with μ given in units of $\mathrm{m^2\,V^{-1}\,s^{-1}}$. Thus, Eq. (6) provides a mobility distribution whose logarithm has a mean and median of μ_0 and a standard deviation of σ. In this way, we can tune the set of parameters (μ_0, σ, and δ) to define an ensemble from which to generate OPV-device replicas, each with a different spatial mobility profile. We present an example mobility profile of one of these replicas in Fig. 1. This mobility profile is generated by sampling an ensemble with the parameters ($\mu_0 = -8.0$, $\sigma = 0.7$, $\delta = 3$ nm). Since many such effectively 1D conducting pathways exist in real OPVs, by averaging over many of these replicas, we can then draw conclusions about the effects of structural disorder on device performance.

Perhaps the single biggest drawback of this approach is that it is still limited to 1D carrier transport. Thus, our method cannot account for the fact that carriers in real devices are not required to translate through low-mobility regions in 1D, but may instead move in three dimensions to find a more continuous pathway of relatively high mobility. We note, however, that charge transport through off-normal dimensions effectively elongates the charge-extraction pathway, which results in a higher probability that charges will be lost to recombination before extraction. Moreover, the presence of dead ends in 3D conduction pathways would result in the buildup of charge carriers, which have no option except to recombine, be transported through the wrong material, or diffuse against their drift vector in order to be extracted. As such, the increased transit time necessary for a charge carrier to find and traverse an OPV device through a continuous pathway can be accounted for as an effective lowering of mobility in the direction of the bulk current flow. Thus, each simulation we perform with a single spatially dependent 1D mobility profile can be thought of as a single, tortuous pathway through a 3D device. It is for this reason that we simulate multiple pathways sampled from the same ensemble and make claims based only on the ensemble-averaged behavior.

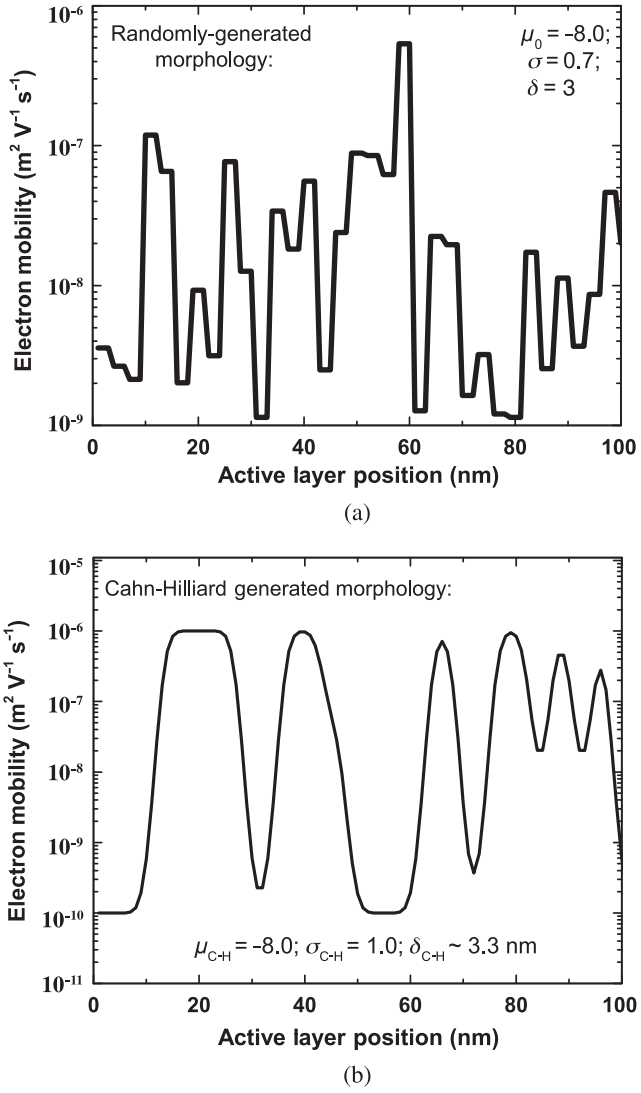

FIG. 1. (a) An example mobility profile of a device replica generated by randomly sampling a mobility ensemble characterized by the parameters $\mu_0 = -8.0$, $\sigma = 0.7$, $\delta = 3$ nm. (b) An example mobility profile of a device replica generated by sampling from a Cahn-Hilliard morphology, with $\mu_{CH} = -8.0$, $\sigma_{CH} = 1.0$, and average $\delta_{CH} \approx 3.3$ nm (CH $\epsilon = 1.6 \times 10^{-5}$).

2. 1D mobility profiles built from Cahn-Hilliard morphologies

Since the mobility profiles generated by our random distribution may or may not be representative of what a carrier encounters in a working device, we also investigated a second way of generating spatially disordered mobility profiles. Our second method is based on the CH model, which is used to describe the spontaneous phase separation of binary fluids [35]. We note that the CH formalism has been used in the past to model the spatial structure of the components in bulk heterojunction solar cells [47–49]. Our choice to also generate mobility profiles via the CH formalism allows us to further test the effects of spatial disorder on device performance, by seeing if the way

mobility profiles are generated has any significant effect on the results. Thus, we also utilized an ensemble of mobility profiles generated from cross sections of morphologies determined by solving the Cahn-Hilliard equation [35]:

$$\frac{\partial C}{\partial t} = D\nabla^2(C^3 - C - \epsilon\nabla^2 C). \tag{7}$$

In this equation, C is the spatial composition of the binary mixture, which varies from one pure component to another such that $C(x, y) \in [-1, 1]$. We utilize 1D slices through these morphologies as a means to generate 1D mobility profiles with randomized regions of enhanced and diminished mobility. Details of our CH calculations are given in the Supplemental Material [43].

The values of the phases generated from the solution to Eq. (7) vary in value from -1 to 1, allowing us to generate the ith replica mobility profile as

$$\mu_i(x) = 10^{\mu_{\mathrm{CH}} + C(x,i)\sigma_{\mathrm{CH}}}. \tag{8}$$

In this expression, σ_{CH} and μ_{CH} are analogous to those used in Eq. (6) with $\mu_i(x)$ given in units of $\mathrm{m^2\,V^{-1}\,s^{-1}}$. In Eq. (6), σ is the standard deviation of the mobility distribution from which mobility profiles are generated, and thus sets the range of possible mobility values that could be found in the ensemble of replica devices. In Eq. (8), σ_{CH} is a multiplicative factor that also sets the range of possible mobility values. The quantity μ_{CH} also serves a corresponding role as μ_0 in Eq. (6) as the midpoint around which a distribution of mobility values may be found.

The mobility profiles generated via Eq. (8) differ from those generated by Eq. (6) in two important ways. First, the mobility profiles obtained from Cahn-Hilliard morphologies exhibit a relatively smooth variation in mobility, as opposed to the abrupt changes in our randomly sampled mobility profiles (see Fig. 1). Second, the CH mobility profiles generated by Eq. (8) do not possess a single, constant feature size δ in contrast to those generated by Eq. (6) that have δ as an explicit and adjustable parameter. The average size of the compositional domains of Cahn-Hilliard morphologies is determined by the interfacial energy term ϵ in Eq. (7). In CH calculations, a lower interfacial energy results in a larger interfacial surface area and thus smaller average domain sizes. Therefore, by altering ϵ, we may generate mobility profiles with a varying average domain size, in much the same way that δ is utilized in our random mobility sampling method.

Once the value of ϵ is chosen, we determine the average domain size of our Cahn-Hilliard generated morphologies δ_{CH} by calculating their radial-pair distance distribution function

$$P(r) = \frac{2}{N(N-1)} \sum_{j>k}^{N} \sum_{k}^{N-1} \delta(r - r_{jk}). \tag{9}$$

The average domain size δ_{CH} is then determined as the distance at which $P(r) = 0.5$ [47]. Thus, the CH formalism provides a second, independent way to generate an ensemble of tunable mobility profiles that can be used to understand the effects of structural order in DD simulations.

III. RESULTS AND DISCUSSION

We begin by using both of our methods to generate ensembles of spatially varying mobility profiles to understand the effects of spatial disorder in drift-diffusion simulations. The initial ensemble of mobility profiles we examined from our random distribution method is characterized by parameters $\mu_0 = -8.0$, $\sigma = 0.7$, and $\delta = 3$ nm. An example of one such spatially variable mobility profile is presented in Fig. 1(a). For our initial Cahn-Hilliard mobility profiles, we sampled a CH morphology that had an average feature size of $\delta_{\mathrm{CH}} \approx 3.3$ nm, corresponding to an ϵ value of 1.6×10^{-5}. We then used those cross sections to generate CH mobility profiles that varied around a central mobility value of 10^{-8} $\mathrm{m^2\,V^{-1}\,s^{-1}}$ and range with composition by 2 orders of magnitude ($\mu_{\mathrm{CH}} = -8.0$, $\sigma_{\mathrm{CH}} = 2.0$). For further details on our Cahn-Hilliard simulations, see the Supplemental Material [43].

Once the two ensembles are generated, we then solved the DD equations for each mobility profile using the boundary conditions collected in Table I to generate the J-V characteristics of 1000 device replicas for each method. We present a sample of 100 of these replica devices' J-V characteristics for each method in Figs. 2(a) and 2(b) for the randomly generated and Cahn-Hilliard calculated profiles, respectively. Each device replica (i.e., each distinct spatially variable mobility profile) exhibits a different short-circuit current (J_{SC}), open-circuit voltage (V_{OC}), and fill factor (FF). Many of the replicas have J-V characteristics that do not appear diodic and thus lead to reduced OPV efficiency in the ensemble average. In particular, the spatial disorder in some of these replica devices produces the so-called "S curve," in which there is an inflection point in the fourth J-V quadrant that leads to a particularly poor fill factor and thus poor power-conversion efficiency [50].

To understand precisely how spatial disorder affects OPV devices, we examine the average J-V curve for both methods' ensembles in Fig. 2(c). For comparison, Fig. 2(c) also includes the calculated J-V curve of a "pristine" device (solid black curve). The pristine device is characterized by a uniform mobility profile whose mobility value is chosen to equal the mean of the distribution from which the device replicas are generated (i.e., $\mu_n = \mu_p = 10^{-8}$ $\mathrm{m^2\,V^{-1}\,s^{-1}}$). Clearly, even though the average mobilities of both the ensemble devices and the pristine device are the same, the inclusion of spatial mobility disorder leads to a decrease in device performance. In particular, both the fill factor and short-circuit current of the spatially disordered devices suffer in comparison to their pristine counterpart. The open-circuit voltage of the ensemble-averaged spatially disordered devices, however, shows no decrease compared to the pristine device, an observation that we rationalize below.

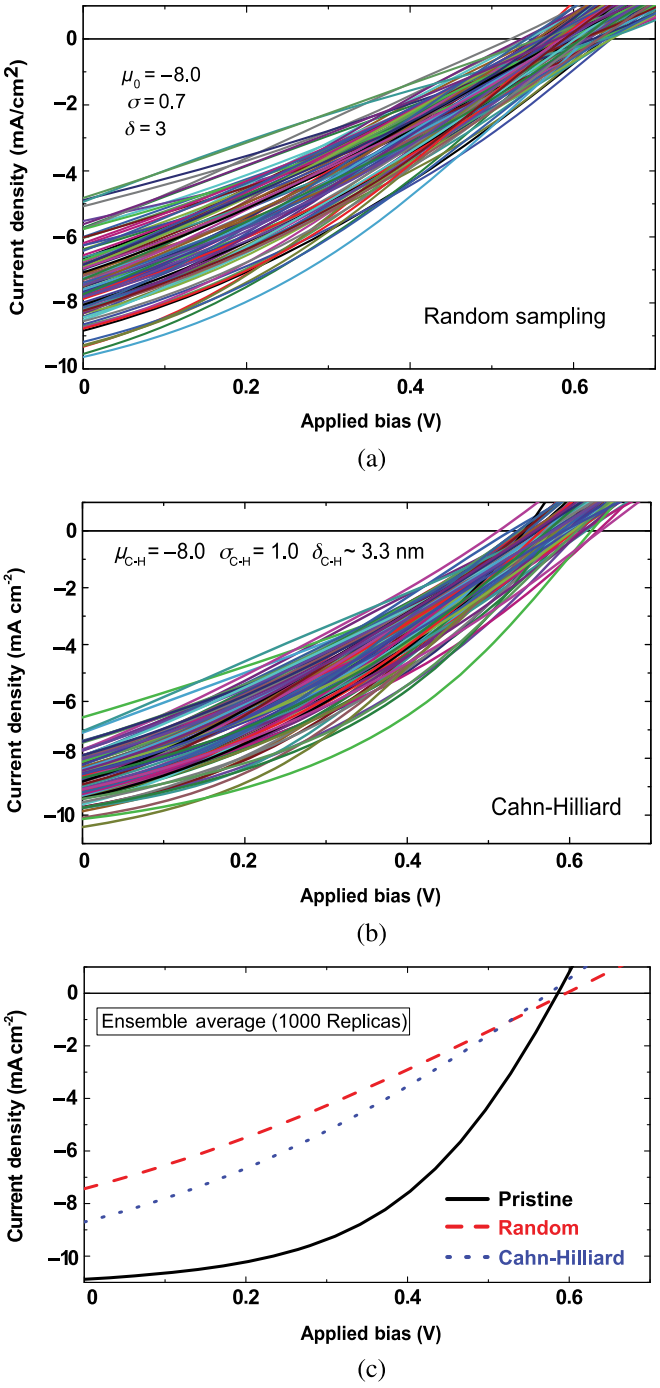

FIG. 2. (a) A collection of J-V characteristics for an ensemble of replicas randomly generated via the random mobility distribution method using the ensemble parameters $\mu_0 = -8.0$, $\sigma = 0.7$, and $\delta = 3$ nm. (b) A collection of J-V characteristics for an ensemble of replicas sampled from Cahn-Hilliard morphologies with $\mu_{CH} = -8.0$, $\sigma_{CH} = 1.0$, and average $\delta_{CH} \approx 3.3$ nm. (c) The ensemble-averaged J-V characteristics for both methods (red-dashed curve for random mobility profiles; blue-dotted curve for CH generated profiles). For comparison, the solid-black curve shows J-V characteristic of a nondisordered, "pristine" device with ($\mu_n = \mu_p = 10^{-8}$ m^2 V^{-1} s^{-1} throughout the active layer).

A. The effects of the range of disordered mobilities on ensemble-averaged device behavior

Now that we have seen the detrimental effects of spatial disorder on device performance, we can examine how altering the type and degree of disorder affects the device physics. The σ and σ_{CH} parameters define the range of possible mobilities and thus the degree of disorder in a given replica. We illustrate the effect of changing the degree of disorder parameter on device performance in Figs. 3(a) and 3(b), which show ensemble-averaged J-V curves with different values of σ and σ_{CH}, respectively. All of these ensembles are chosen to have the same average mobility and spatial feature size, but each has a different range of potential mobility values. For both sampling methods examined, increasing the degree of spatial disorder by increasing the range of possible mobilities monotonically decreases the ensemble-averaged device performance.

To more thoroughly examine how changes in the degree of disorder affect device performance, Figs. 4(a) and 4(b) illustrate trends in the pertinent figures of merit for device performance as a function of σ and σ_{CH}, respectively. In these plots, the device figures of merit are displayed as the fraction of their value relative to the pristine (i.e., uniform

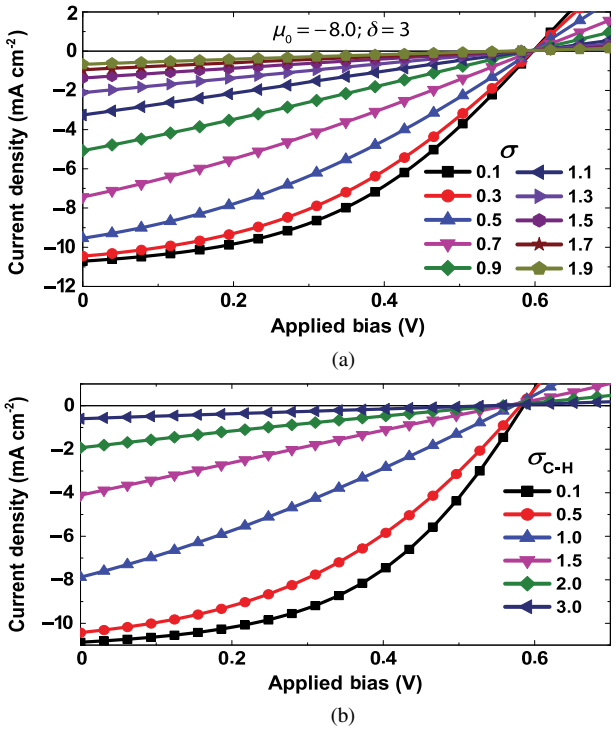

FIG. 3. Ensemble-averaged J-V characteristics for several series of replica devices. Each curve is the average of 1000 replicas. (a) Mobility profiles generated from the random distribution method with $\mu_0 = -8.0$ and $\delta = 3$ nm but different values of the degree of disorder parameter σ, which ranges from 0.1 to 1.9 in steps of 0.2. (b) Mobility profiles generated from CH morphologies with $\epsilon = 1.6 \times 10^{-5}$ and thus $\delta_{CH} \approx 3.3$ nm but different values of σ_{CH} ranging from 0.1 to 3.0 as indicated.

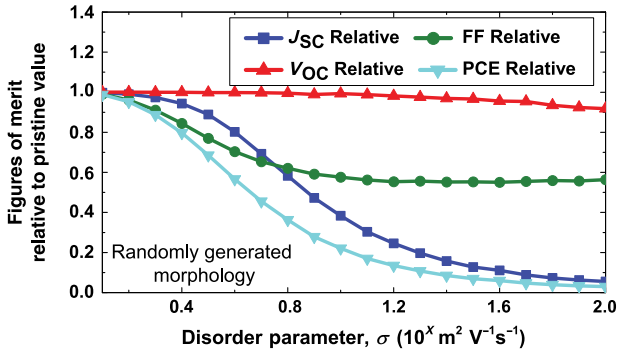

(a)

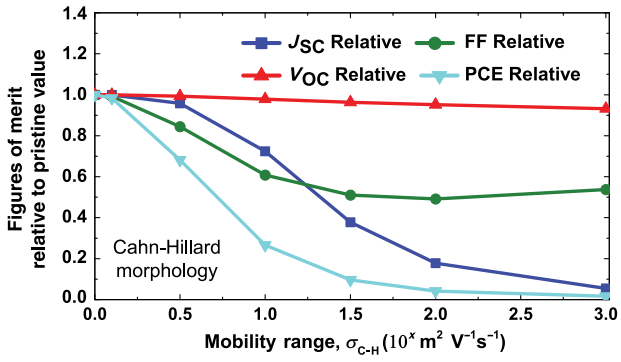

(b)

FIG. 4. Relevant figures of merit of ensemble-averaged J-V characteristics for the series of replicas presented in Fig. 3 as a fraction of a pristine device's taken as (a) the disorder parameter for the random mobility distribution method σ is increased from 0.1 to 2.0, and (b) the disorder parameter σ_{CH} for the Cahn-Hillard morphology method is varied from 0.1 to 3.0.

mobility profile) device with the same average mobility. Both the J_{SC} and the FF drop in value as the degree of disorder parameter is increased, resulting in a concomitant drop in power conversion efficiency. Although V_{OC} does eventually begin to decrease for high values of σ and σ_{CH}, this decrease is very small compared to the drops in J_{SC} and FF. In fact, by the time σ is large enough to see a significant effect of disorder on V_{OC}, the values of J_{SC} and FF are so incredibly low that the device is already effectively nonfunctional. Thus, V_{OC} can be considered essentially impervious to disorder for the degrees of disorder that are representative of typical performance OPV devices.

Of particular interest is the similarity of performance trends between mobility ensembles generated by random sampling [Fig. 4(a)] and those generated by sampling Cahn-Hilliard morphologies [Fig. 4(b)]. The distributions of possible mobilities for both of these sampling methods are decidedly different. In the former case, the ensembles' mobilities are normally distributed around a mean value, μ_0 of 10^{-8} m^2 V^{-1} s^{-1}, with values that range from $\sim 10^{-6}$ to $\sim 10^{-10}$ m^2 V^{-1} s^{-1}. In the latter case, the ensembles' mobilities are roughly bimodally distributed, with the majority of mobilities distributed near 10^{-6} and 10^{-10} m^2 V^{-1} s^{-1} (see Supplemental Material for histograms of these distributions) [43]. This is a direct result of the fact that Cahn-Hilliard morphologies vary from the extremes of one pure component to the other. The fact that these two very different mobility distributions lead to essentially the same result suggests that the exact shape of the mobility distribution being sampled is less important to device performance than the *range* of possible mobility values and the way such values are spatially distributed, as we discuss further below.

1. The effects of spatial mobility disorder on J_{SC} and FF

The large decrease in device performance with increasing disorder arises from lower limits of the possible device figures of merit in the case of extreme disorder. The lower limit for J_{SC} is clearly zero, and we see the device current approaching this as σ or σ_{CH} increases. This results from the fact that for high values of the disorder parameter, a significant fraction of the replicas have occasional domains of exceptionally low mobility ($\sim 10^{-11}$ to 10^{-12} m^2 V^{-1} s^{-1}). These domains are so limiting to charge transport that charges cannot be extracted before they inevitably recombine, resulting in essentially zero net photocurrent. The lower limit for the FF with increasing disorder appears to be roughly 0.25. At this point, the average J-V characteristic of the devices ceases to be diodic and instead resembles a resistor with a nearly linear J-V relationship. This is because for high values of the disorder parameter, the presence of low-mobility domains dominates the overall charge transport, resulting in devices with low conductivity and thus high resistivity.

To better elucidate the way spatial disorder impacts the performance of an ensemble of devices, in Fig. 5 we present histograms of the figures of merits of an ensemble of devices whose mobility profiles are generated via the random sampling method (we present the corresponding histograms for the CH method in the Supplemental Material [43]). Because the random sampling and Cahn-Hillard methods produce qualitatively identical results and lead to the same conclusions, in what follows we show only the data for the random sampling method in the main text without loss of generality. Figure 5 shows that both the J_{SC} and the FF exhibit skewed distributions that cause their means to be lower than their medians. This skewness is perhaps not surprising given that there is an effective upper bound to both the J_{SC} and the FF. The fill factor has traditionally been seen as a measure of how beneficial the morphology of the device is to charge transport, and clearly the pristine morphology exhibits the highest possible FF for the chosen set of DD parameters. Thus, inserting regions of low mobility within a pristine material lowers the fill factor. Conversely, it is hard to imagine that inserting occasional regions of relatively high mobility could drastically improve charge transport if there are low-mobility domains elsewhere in the transport pathway. These same arguments also hold for the J_{SC}, explaining

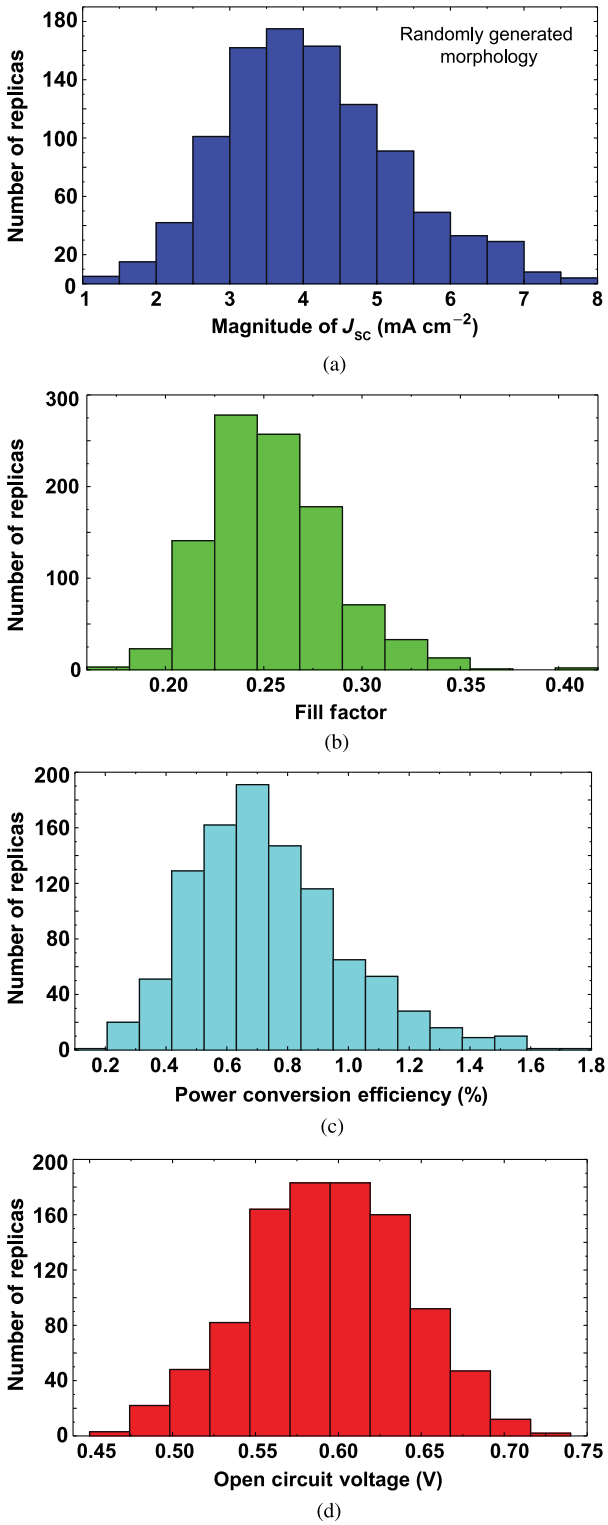

FIG. 5. Histograms illustrating the distribution of (a) the short-circuit current, (b) the fill factor, (c) the power conversion efficiency, and (d) the open-circuit voltage for individual device replicas sampled from the randomly generated spatial mobility distribution ensemble of Fig. 1(a) ($\mu_0 = -8.0$, $\sigma = 0.7$, $\delta = 3$ nm); see the Supplemental Material for the corresponding plots for spatially disordered mobility replicas generated by the CH method [43].

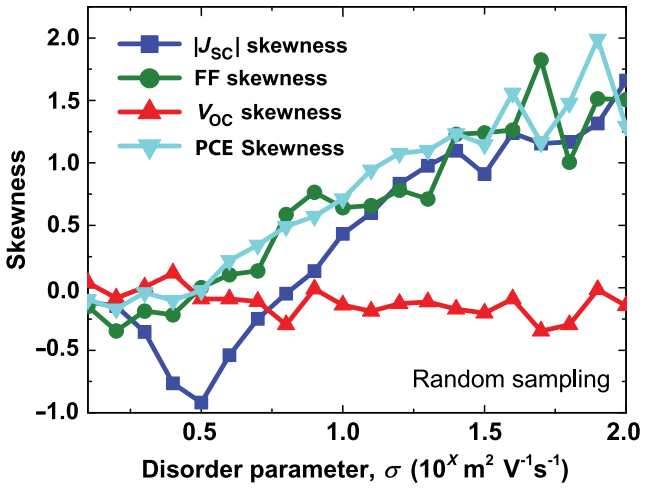

FIG. 6. Skewness of device replicas' figures of merit as a function of the disorder parameter σ [same randomly generated mobility replicas whose individual properties and ensemble-averaged behavior are summarized in Figs. 2(a)–5].

why the J_{SC} and FF have an effective upper bound (corresponding to a pristine device with uniform carrier mobility), which results in a skewed distribution that biases the average towards lower values.

Figure 6 summarizes the behavior of the skewness of the J_{SC} (dark-blue curve), FF (green curve), and PCE (light-blue curve) distributions for different randomly generated mobility ensembles with changing disorder parameter (σ). The skewness of a population can be estimated from a sample of the population by

$$\gamma = \frac{m_3}{s^3} = \frac{\frac{1}{n}\sum_{i=1}^{n}(x_i - \bar{x})^3}{\left[\frac{1}{n-1}\sum_{i=1}^{n}(x - \bar{x})^2\right]^{3/2}}, \tag{10}$$

where m_3 is the sample third central moment and s is the sample standard deviation of the population of values. We emphasize that this standard deviation corresponds to the sample of the values of the device figures of merit (J_{SC}, FF, and V_{OC}) and not the standard deviation of the mobility distribution from which the sample of replica devices is generated. For lower values of the disorder parameter σ, both the J_{SC} and FF distributions are negatively skewed; that is, they have a tail towards lower values and their mean is less than their median. At higher values of σ, the direction of this tail reverses and the distributions become positively skewed. This reversal in skewness results from a change in the replicas' performance from being upper-bound dominated to lower-bound dominated. For both the short-circuit current and fill factor, the lower bound corresponds to zero current flowing or the 0.25 effectively linear FF in the device as a result of the presence of low-mobility regions in the average mobility profile.

2. *The effects of spatial mobility disorder on V_{OC}*

Figures 5 and 6 also examine the skewness of the distribution of open-circuit voltages for the randomly

generated spatially disordered mobility replicas (red curve, bars), which is expected to depend primarily on the nature of carrier recombination [51]. For all values of σ that we explore, the V_{OC} distribution has a skewness of nearly zero and thus follows a nearly normal distribution. The normal distribution of V_{OC} results from the fact that we are utilizing a Langevin recombination mechanism of the form

$$R(x) = \frac{q}{\epsilon_r \epsilon_0}[\mu_n(x) + \mu_p(x)]n(x)p(x), \qquad (11)$$

which depends directly on the mobility. Despite the explicitly linear dependence in Eq. (11), we note that recombination is actually nonlinearly dependent on mobility since the electron and hole densities are implicitly functions of their respective carrier mobilities. Thus, decreasing the mobility for either carrier in a particular spatial region leads to a locally diminished recombination rate, and therefore a lower recombination term in Eq. (2). This same low mobility, however, also leads to a buildup of charge in that spatial region, which leads to a locally increased recombination rate.

This subtle balance between carrier buildup and carrier recombination can result in replicas with either enhanced recombination or lowered recombination, which by the central-limit theorem we expect to be normally distributed. This results in an ensemble with approximately the same average amount of recombination per device as a nondisordered device. Since V_{OC} occurs at the voltage for which the recombination rate equals the generation rate (and since the generation rate is constant for all replicas), it follows that ensemble-averaged V_{OC} should be roughly the same as that of a nondisordered device. As a result, the average V_{OC} is relatively impervious to increasing spatial mobility disorder. This finding is in stark contrast to what happens in the case of energetic disorder, where previous studies have found that V_{OC} decreases with increasing energetic disorder [15]. The DD simulations we present here consider only structural disorder, so we can conclude that V_{OC} is not affected by structural disorder, and should be thought of as susceptible only to the energetic disorder that inherently accompanies structural disorder and the way this energetic disorder affects the recombination kinetics.

We note that our assumption of a Langevin recombination mechanism has been shown in previous studies to overestimate the recombination rate in DD simulations relative to experimental OPV devices [33,52,53]. As such, drift-diffusion studies which employ such a mechanism typically include a recombination reduction factor, which typically ranges from 10^{-1} to 10^{-3} [54,55]. Our simulations employ a relatively mild reduction factor of 10^{-1}, which leads to a relatively large amount of recombination and thus somewhat diminished fill factors. Utilizing a stronger recombination reduction factor would allow our simulated devices to experience greater structural disorder (that is, larger values of σ) before manifesting a comparable degree of performance degradation. But no matter what the degree of recombination, the general conclusion of structural disorder's deleterious effects on device performance holds, and may simply be manifest to a lesser degree in instances of lower recombination.

B. The effects of the spatial-disorder length scale on OPV device performance

We next turn our investigation to how the length scale of spatial disorder affects device performance. X-ray diffraction and various microscopy measurements have indicated that the polymers and fullerenes in a BHJ phase segregate into domains with sizes on the order of several nanometers, with amorphous and potentially intermixed regions surrounding the domains [27–31]. To investigate the effects of the phase-separation (and thus the spatial-disorder) length scale on device performance, we varied the size of the mobility regions in our ensembles from 2 to 20 nm. We do not consider disorder length scales below 2 nm since smaller length scales would correspond to the diameter of single fullerene molecules, thus representing a lower bound to the morphological granularity in a real device [56].

Figure 7 illustrates the effect of changing the simulated domain feature size δ for the randomly generated mobility profiles on the ensemble-averaged figures of merit. As above, these are presented as a fraction of the figure of merit for a pristine device with no structural disorder. (We note that tuning the size scale of the spatial disorder is less direct with the CH method, as the average length scale δ_{CH} depends in a nonlinear way on the ϵ parameter in Eq. (7); see the Supplemental Material for details [43]). As we saw above for the degree of disorder, V_{OC} is relatively unaffected by the introduction of structural features, and has nearly the same average value for all spatially disordered length scales relative to a nondisordered, pristine device. In contrast, both the J_{SC} and the FF are negatively impacted

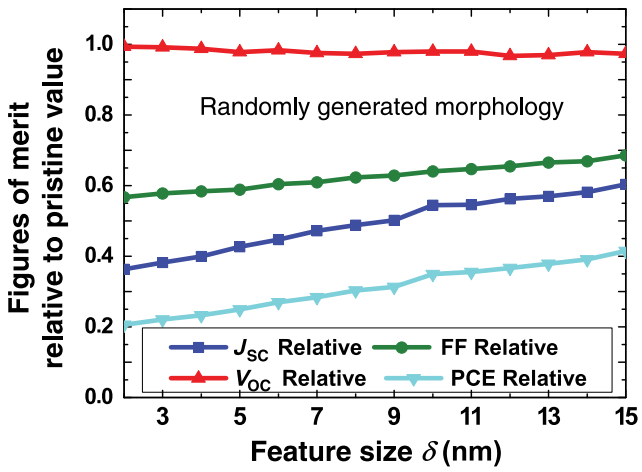

FIG. 7. Relevant figures of merit for the ensemble-averaged J-V characteristics presented in Fig. 3(a) as a fraction of the pristine device's but as the spatial feature size δ in the randomly generated profile ensemble is increased from 2 to 15 nm.

by the inclusion of discrete mobility regions, and they are more impacted the smaller the features become. Clearly, the fact that real OPV devices are designed to have BHJs with structure on ~10 nm length scales reinforces the idea that structural disorder is too important to be overlooked in DD modeling of OPV devices.

To further examine the effects of structural disorder on device performance, we also simulated an ensemble of devices characterized by $\mu_0 = -8.0$, $\sigma = 0.7$, and $\delta = d = 100$ nm, the entire device thickness. An ensemble characterized by these parameters results in individual mobility profiles that have a single, uniform value for their mobility. Thus each device replica will have a randomly assigned mobility but no spatial disorder. This ensemble thus decouples the effects of simple mobility disorder (σ) from structural mobility disorder (δ), which is present only in ensembles with structural features that are smaller than the thickness of the device. Figure 8 compares the averaged results for this ensemble (red circles, curve) to that of a well-disordered ensemble with $\mu_0 = -8.0$, $\sigma = 0.7$, $\delta = 3$ nm (blue triangles and curve). The data show that the inclusion of spatially varying random mobilities diminishes the average performance of the device to a much greater extent than a simple ensemble of random, uniform mobilities. This suggests that the negative impacts of structural disorder are not the result of low-mobility replicas alone. Rather, it is the fact that spatial disorder includes regions of both high and low mobility that has a significant detrimental effect on device performance. Thus, the reason device performance becomes so diminished at larger values of σ is because the mobility difference between the high- and low-mobility regions becomes more drastic; in other words, the impact that spatial disorder has on device performance becomes larger.

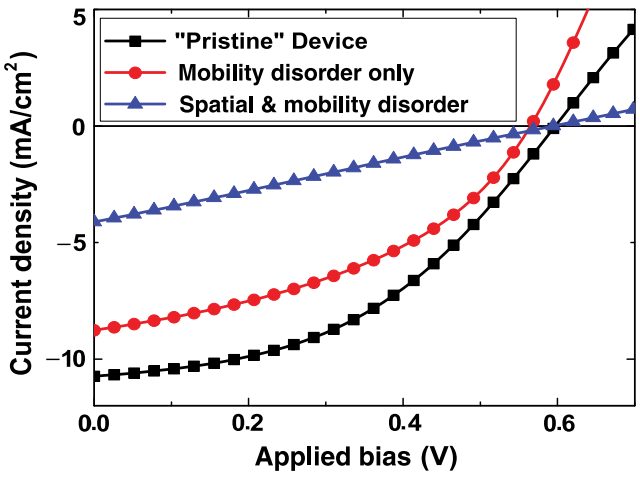

FIG. 8. J-V curves comparing a randomly generated structurally disordered ensemble (blue triangles) with an ensemble of structurally pristine devices with only mobility disorder (red circles; see text for details). Note that although both ensembles' performance diminishes as a result of the inclusion of disorder, the inclusion of structural disorder leads to a much more severe drop in performance.

C. The effects of spatial disorder on the shape of J-V curve

As pointed out above, the introduction of spatial disorder can lead to an S-shaped J-V curve with a very poor FF. Using the same DD modeling approach employed here, we have illustrated in a previous paper how such S-shaped J-V characteristics can be produced by devices that have diminished carrier mobility near an extraction contact [57]. Our previous paper assumed a pristine mobility profile except for a precipitous drop in mobility for electrons near the cathode contact. In the current study, in which mobility profiles are either randomly generated or taken from Cahn-Hilliard calculations, it is easily possible for a replica to have a mobility profile similar to that of our previous work, with low-mobility domains near one or both of the extraction contacts.

When we analyzed our individual randomly generated and CH mobility profiles, we found that those with a calculated S-shaped J-V curve are indeed almost all characterized by a region of low mobility near one of the extraction contacts. Of particular note, not all of these replicas had the low-mobility region contiguous with the extraction contact; instead, in several instances of replicas with S-shaped J-V curves, the low-mobility regions are up to 20 nm away from the contact. Of course, Fig. 2 shows that the number of replicas that result in S-shaped J-V curves are not sufficient to cause the ensemble-averaged performance to deviate terribly far from typical diodic behavior. However, it is reasonable to assume that if a significant number of replicas are characterized by diminished mobility near an extraction contact, the resulting ensemble-averaged J-V characteristic would exhibit an overall S curve. Thus, the apparently random occurrence of S curves in experimental devices is dependent on an ensemble morphology that results in poor mobility for a carrier near its extraction contact: S curves occur when there is a particular problem maintaining mobility near the extraction contact (e.g., via undesirable vertical phase separation), or when the inherent structural disorder in an OPV device happens to leave low-mobility regions near the contacts along the majority of the effectively 1D conduction pathways traversed by the carriers in a particular BHJ geometry.

IV. CONCLUSIONS

In this work, we have used drift-diffusion modeling to examine the effects of structural disorder on the performance of BHJ organic photovoltaic devices. We argued that it is possible to study the effects of 3D spatial disorder in an OPV device via an ensemble average of 1D drift-diffusion models. This is because photogenerated carriers in real 3D devices must traverse a relatively small number of effectively 1D tortuous, high-conductivity paths to reach the

device electrodes. As these carriers encounter grain boundaries, dead ends, or cul-de-sacs along their journey, they effectively lose mobility in the direction of the bulk current. Our approach to accounting for the effects of this disorder involves modeling many replica pathways with mobility profiles either randomly generated from an ensemble mobility distribution or generated via Cahn-Hilliard modeling. Using this approach, we investigated how the range of mobilities sampled and the size of typical mobility features affected the overall (ensemble-average) device performance.

Based on looking at averages and distributions of 1D-device models with different disorder parameters, we have shown that the short-circuit current and fill factor are negatively affected by the inclusion of structural disorder, but the open-circuit voltage is nearly impervious to disorder's debilitating effects. This nondependence of the open-circuit voltage on structural disorder stands in strong contrast to energetic disorder, which has been shown to have a profound detrimental effect on V_{OC} [15]. The strong dependence of the J_{SC} and the FF on structural disorder results from the fact that these figures of merit have effective lower and upper limits for particular mobility profiles, thus forcing an asymmetry in the ensemble that is averaged to simulate the device performance. We also have found that the inclusion of structural disorder is imperative if the OPV architecture in question has feature sizes of a few nm, which is indeed the case for nearly every experimental BHJ device. Finally, we found that no matter how the individual spatially varying mobility profiles are generated, the results we obtained are the same, indicating that all off the effects discussed above are universal features of spatial disorder and are not dependent on the microscopic details.

As previously discussed, our method for approximating structural disorder is still limited by 1D charge transport. We are thus missing some of the correlated distribution of charge-conducting materials present in a true 3D BHJ architecture. We hope to further refine our modeling of structural disorder by eventually extending our simulations to higher-dimensionality mobility profiles that include the carriers' ability to conduct perpendicular to bulk current flow. We also plan to couple spatial disorder with energetic disorder to better understand the interplay of these two different types of disorder on BHJ device performance. Until such subsequent drift-diffusion studies are carried out, we believe that this 1D study and analysis provide strong evidence that structural disorder is of paramount consideration for the modeling and development of OPV devices.

ACKNOWLEDGMENTS

The authors acknowledge support from the Molecularly Engineered Energy Materials (MEEM), an Energy Frontier Research Center funded by the U.S. Department of Energy, Office of Science, Office of Basic Energy Sciences under Award No. DE-SC0001342, and from the National Science Foundation under Grants No. 1112569 and No. 1510353.

[1] Huiqiong Zhou, Yuan Zhang, Cheng-Kang Mai, Samuel D. Collins, Guillermo C. Bazan, Thuc-Quyen Nguyen, and Alan J. Heeger, Polymer homo-tandem solar cells with best efficiency of 11.3%, Adv. Mater. **27**, 1767 (2015).

[2] Jingbi You, Letian Dou, Ken Yoshimura, Takehito Kato, Kenichiro Ohya, Tom Moriarty, Keith Emery, Chun-Chao Chen, Jing Gao, Gang Li, and Yang Yang, A polymer tandem solar cell with 10.6% power conversion efficiency, Nat. Commun. **4**, 1446 (2013).

[3] Sylvia J. Lou, Jodi M. Szarko, Tao Xu, Luping Yu, Tobin J. Marks, and Lin X. Chen, Effects of additives on the morphology of solution phase aggregates formed by active layer components of high-efficiency organic solar cells, J. Am. Chem. Soc. **133**, 20661 (2011).

[4] Inchan Hwang and Neil C. Greenham, Modeling photocurrent transients in organic solar cells, Nanotechnology **19**, 424012 (2008).

[5] Wolfgang Tress, Karl Leo, and Moritz Riede, Optimum mobility, contact properties, and open-circuit voltage of organic solar cells: A drift-diffusion simulation study, Phys. Rev. B **85**, 155201 (2012).

[6] Wolfgang Tress and Olle Inägans, Simple experimental test to distinguish extraction and injection barriers at the electrodes of (organic) solar cells with S-shaped current-voltage characteristics, Sol. Energy Mater. Sol. Cells **117**, 599 (2013).

[7] James A. Barker, Catherine M. Ramsdale, and Neil C. Greenham, Modeling the current-voltage characteristics of bilayer polymer photovoltaic devices, Phys. Rev. B **67**, 075205 (2003).

[8] Martin T. Neukom, Simon Züfle, and Beat Ruhstaller, Reliable extraction of organic solar cell parameters by combining steady-state and transient techniques, Org. Electron. **13**, 2910 (2012).

[9] Inchan Hwang, Christopher R. McNeill, and Neil C. Greenham, Drift-diffusion modeling of photocurrent transients in bulk heterojunction solar cells, J. Appl. Phys. **106**, 094506 (2009).

[10] Alexander Wagenpfahl, Daniel Rauh, Moritz Binder, Carsten Deibel, and Vladimir Dyakonov, S-shaped current-voltage characteristics of organic solar devices, Phys. Rev. B **82**, 115306 (2010).

[11] Wolfgang Tress, Karl Leo, and Moritz Riede, Influence of hole-transport layers and donor materials on open-circuit voltage and shape of *I-V* curves of organic solar cells, Adv. Funct. Mater. **21**, 2140 (2011).

[12] Wolfgang Tress, Annette Petrich, Markus Hummert, Moritz Hein, Karl Leo, and Moritz Riede, Imbalanced mobilities causing S-shaped IV curves in planar heterojunction organic solar cells, Appl. Phys. Lett. **98**, 063301 (2011).

[13] Andreas Petersen, Thomas Kirchartz, and Thomas A. Wagner, Charge extraction and photocurrent in organic bulk heterojunction solar cells, Phys. Rev. B **85**, 045208 (2012).

[14] Siebe L. M. van Mensfoort, S. I. E. Vulto, Rene A. J. Janssen, and Reinder Coehoorn, Hole transport in polyfluorene-based sandwich-type devices: Quantitative analysis of the role of energetic disorder, Phys. Rev. B **78**, 085208 (2008).

[15] James C. Blakesley and Dieter Neher, Relationship between energetic disorder and open-circuit voltage in bulk heterojunction organic solar cells, Phys. Rev. B **84**, 075210 (2011).

[16] Thomas Kirchartz, Bart E. Pieters, James Kirkpatrick, Uwe Rau, and Jenny Nelson, Recombination via tail states in polythiophene:fullerene solar cells, Phys. Rev. B **83**, 115209 (2011).

[17] Nico Christ, Siegfried W. Kettlitz, Simon Züfle, Sebastian Valouch, and Uli Lemmer, Nanosecond response of organic solar cells and photodiodes: Role of trap states, Phys. Rev. B **83**, 195211 (2011).

[18] Janine Fischer, Johannes Widmer, Hans Kleeman, Wolfgang Tress, Christian Koerner, Moritz Riede, Koen Vandewal, and Karl Leo, A charge carrier transport model for donor-acceptor blend layers, J. Appl. Phys. **117**, 045501 (2015).

[19] Almantas Pivrikas, Niyazi Serdar Sariciftci, Gytis Juška, and Ronald Österbacka, A review of charge transport and recombination in polymer/fullerene organic solar cells, Prog. Photovoltaics **15**, 677 (2007).

[20] Roderick C. I. MacKenzie, Christopher G. Shuttle, Michael L. Chabinyc, and Jenny Nelson, Extracting microscopic device parameters from transient photocurrent measurements of P3HT:PCBM solar cells, Adv. Energy Mater. **2**, 662 (2012).

[21] Zhibing Wang, Michael G. Helander, Mark T Greiner, Jacky Qiu, and Zheng-Hong Lu, Carrier mobility of organic semiconductors based on current-voltage characteristics, J. Appl. Phys. **107**, 034506 (2010).

[22] Jordan C. Aguirre, Christopher Arntsen, Samuel Hernandez, Rachel Huber, Alexandre M. Nardes, Merissa Halim, Daniel Kilbride, Yves Rubin, Sarah H. Tolbert, Nikos Kopidakis, Benjamin J. Schwartz, and Daniel Neuhauser, Understanding local and macroscopic electron mobilities in the fullerene network of conjugated polymer-based solar cells: Time-resolved microwave conductivity and theory, Adv. Funct. Mater. **24**, 784 (2014).

[23] Henning Sirringhaus, P. J. Brown, R. H. Friend, M. M. Nielsen, K. Bechgaard, B. M. W. Langeveld-Voss, A. J. H. Spiering, R. A. J. Janssen, E. W. Meijer, P. Herwig, and D. M. de Leeuw, Two-dimensional charge transport in self-organized, high-mobility conjugated polymers, Nature (London) **401**, 685 (1999).

[24] Marta Mas-Torrent, D. den Boer, M. Durkut, P Hadley, and Albert P. H. J. Schenning, Field effect transistors based on poly(3-hexylthiophene) at different length scales, Nanotechnology **15**, S265 (2004).

[25] Yi-Kang Lan and Ching-I Huang, A theoretical study of the charge transfer behavior of the highly regioregular poly-3-hexylthiophene in the ordered state, J. Phys. Chem. B **112**, 14857 (2008).

[26] Thuc-Quyen Nguyen, Junjun Wu, Vinh Doan, Benjamin J. Schwartz, and Sarah H. Tolbert, Control of energy transfer in oriented conjugated polymer-mesoporous silica composites, Science **288**, 652 (2000).

[27] Uladzimir Zhokhavets, Tobias Erb, Harald Hoppe, Gerhard Gobsch, and Niyazi Serdar Sariciftci, Effect of annealing of poly(3-hexylthiophene)/fullerene bulk heterojunction composites on structural and optical properties, Thin Solid Films **496**, 679 (2006).

[28] Svetlana S. van Bavel, Erwan Sourty, Gijsbertus de With, and Joachim Loos, Three-dimensional nanoscale organization of bulk heterojunction polymer solar cells, Nano Lett. **9**, 507 (2009).

[29] Ji Sun Moon, Jae Kwan Lee, Shinuk Cho, Jiyun Byun, and Alan J. Heeger, "Columnlike" structure of the cross-sectional morphology of bulk heterojunction materials, Nano Lett. **9**, 230 (2009).

[30] Bertrand Tremolet de Villers, Christopher J. Tassone, Sarah H. Tolbert, and Benjamin J. Schwartz, Improving the reproducibility of P3HT:PCBM solar cells by controlling the PCBM/cathode interface, J. Phys. Chem. C **113**, 18978 (2009).

[31] Wei-Ru Wu, U-Ser Jeng, Chun-Jen Su, Kung-Hwa Wei, Ming-Shin Su, Mao-Yuan Chiu, Chun-Yu Chen, Wen-Bin Su, Chiu-Hun Su, and An-Chung Su, Competition between fullerene aggregation and poly(3-hexylthiophene) crystallization upon annealing of bulk heterojunction solar cells, ACS Nano **5**, 6233 (2011).

[32] Evelyne Knapp, Roger Häeusermann, H. U. Schwarzenbach, and Beat Ruhstaller, Numerical simulation of charge transport in disordered organic semiconductor devices, J. Appl. Phys. **108**, 054504 (2010).

[33] Juliane Kniepert, Ilja Lange, Niels J. van der Kaap, L. Jan Anton Koster, and Dieter Neher, A conclusive view on charge generation, recombination, and extraction in as-prepared and annealed P3HT:PCBM blends: Combined experimental and simulation work, Adv. Energy Mater. **4**, 1301401 (2014).

[34] David J. Eyre, An unconditionally stable one-step scheme for gradient systems (unpublished); available online from http://www.math.utah.edu/~eyre/research/methods/stable.ps; MATLAB code: http://www.math.utah.edu/~eyre/computing/matlab-intro/ch.txt.

[35] Lukasz Bolikowski and Maria Gokieli, Simulating phase transition dynamics on non-trivial domains, in *Parallel Processing and Applied Mathematics*, edited by Roman Wyrzykowski, Jack Dongarra, Konrad Karczewski, and Jerzy Waniewski (Springer, Berlin, Heidelberg, 2014), pp. 510–519, MATLAB code: https://github.com/bolo1729/cahn-hilliard.

[36] Jonathan D. Servaites, Mark A. Ratner, and Tobin J. Marks, Organic solar cells: A new look at traditional models, Energy Environ. Sci. **4**, 4410 (2011).

[37] Leif A. A. Pettersson, Lucimara S. Roman, and Olle Inganäs, Modeling photocurrent action spectra of photovoltaic devices based on organic thin films, J. Appl. Phys. **86**, 487 (1999).

[38] Hermann K. Gummel, Self-consistent iterative scheme for 1-dimensional steady state transistor calculations, IEEE Trans. Electron Devices **11**, 455 (1964).

[39] Donald L. Scharfetter and Hermann K. Gummel, Large-signal analysis of a silicon read diode oscillator, IEEE Trans. Electron Devices **16**, 64 (1969).

[40] Siegfried Selberherr, *Analysis and Simulation of Semiconductor Devices* (Springer, New York, 1984), pp. 208–212.

[41] Christopher M. Snowden, *Semiconductor Device Modeling* (Peter Peregrinus Ltd., London, UK, 1988).

[42] J. Campbell Scott and George G. Malliaras, Charge injection and recombination at the metalorganic interface, Chem. Phys. Lett. **299**, 115 (1999).

[43] See Supplemental Material at http://link.aps.org/supplemental/10.1103/PhysRevApplied.4.034006 for details on Cahn-Hilliard simulations and mobility distributions.

[44] Oleksandr V. Mikhnenko, Hamed Azimi, Markus Scharber, Mauro Morana, Paul W. M. Blom, and Maria Antonietta Loi, Exciton diffusion length in narrow bandgap polymers, Energy Environ. Sci. **5**, 6960 (2012).

[45] R. Joseph Kline, Michael D. McGehee, Ekaterina N. Kadnikova, Jinsong Liu, and Jean M. J. Frechet, Controlling the field-effect mobility of regioregular polythiophene by changing the molecular weight, Adv. Mater. **15**, 1519 (2003).

[46] Thomas D. Anthopoulos, Dago M. de Leeuw, Eugenio Cantatore, Patrick van 't Hof, Jan Alma, and Jan C. Hummelen, Solution processible organic transistors and circuits based on a C-70 methanofullerene, J. Appl. Phys. **98**, 054503 (2005).

[47] Benjamin P. Lyons, Nigel Clark, and Chris Groves, The relative importance of domain size, domain purity and domain interfaces to the performance of bulk-heterojunction organic photovoltaics, Energy Environ. Sci. **5**, 7657 (2012).

[48] Biswajit Ray and Muhammad A. Alam, Random vs regularized OPV: Limits of performance gain of organic bulk heterojunction solar cells by morphology engineering, Sol. Energy Mater. Sol. Cells **99**, 204 (2012).

[49] Olga Wodo and Baska Ganapathysubramanian, Modeling morphology evolution during solvent-based fabrication of organic solar cells, Comput. Mater. Sci. **55**, 113 (2012).

[50] Markus Glatthaar, Moritz Riede, Nicholas Keegan, Kristian Sylvester-Hvid, Birger Zimmermann, Michael Niggemann, Andreas Hinsch, and Andreas Gombert, Efficiency limiting factors of organic bulk heterojunction solar cells identified by electrical impedance spectroscopy, Sol. Energy Mater. Sol. Cells **91**, 390 (2007).

[51] Christopher G. Shuttle, Brian O'Regan, A. M. Ballantyne, Jenny Nelson, Donald D. C. Bradley, and James R. Durrant, Bimolecular recombination losses in polythiophene: Fullerene solar cells, Phys. Rev. B **78**, 113201 (2008).

[52] Christopher M. Proctor, Martijn Kuik, and Thuc-Quyen Nguyen, Charge carrier recombination in organic solar cells, Prog. Polym. Sci. **38**, 1941 (2013).

[53] Girish Lakhwani, Akshay Rao, and Richard H. Friend, Bimolecular recombination in organic photovoltaics, Annu. Rev. Phys. Chem. **65**, 557 (2014).

[54] Carsten Deibel, Alexander Wagenpfahl, and Vladimir Dyakonov, Origin of reduced polaron recombination in organic semiconductor devices, Phys. Rev. B **80**, 075203 (2009).

[55] Timothy M. Burke, Sean Sweetnam, Koen Vandewal, and Michael D. McGehee, Beyond Langevin recombination: How equilibrium between free carriers and charge transfer states determines the open-circuit voltage of organic solar cells, Adv. Energy Mater. **5**, 1500123 (2015).

[56] Rui Qiao, Aaron P. Roberts, Andrew S. Mount, Stephen J. Klaine, and Pu Chun Ke, Translocation of C-60 and its derivatives across a lipid bilayer, Nano Lett. **7**, 614 (2007).

[57] Benjamin Y. Finck and Benjamin J. Schwartz, Understanding the origin of the S-curve in conjugated polymer/fullerene photovoltaics from drift-diffusion simulations, Appl. Phys. Lett. **103**, 053306 (2013).